Dominant role of inverse Cotton-Mouton effect in ultrafast stimulation of magnetization precession in undoped yttrium iron garnet films by 400-nm laser pulses

L. Q. Shen,[1] L. F. Zhou,[2] J. Y. Shi,[1] M. Tang,[3] Z. Zheng,[1] D. Wu,[2] S. M. Zhou,[3] L. Y. Chen,[1] and H. B. Zhao[1,*]

[1]*Shanghai Ultra-precision Optical Manufacturing Engineering Research Center, and Key Laboratory of Micro and Nano Photonic Structures (Ministry of Education), Department of Optical Science and Engineering, Fudan University, Shanghai, 200433, China*

[2]*National Laboratory of Solid State Microstructures, Collaborative Innovation Center of Advanced Microstructures and Department of Physics, Nanjing University, Nanjing, 210093, China*

[3]*Shanghai Key Laboratory of Special Artificial Microstructure Materials and Technology & Physics Department, Tongji University, Shanghai, 200092, China*

(Received 16 March 2018; published 29 June 2018)

Magnetization (***M***) precessions driven by ultrafast laser-induced nonthermal effects are observed in undoped yttrium iron garnet (YIG) films of (100) and (111) orientations using pump-probe time-resolved magneto-optical Kerr effect. The ***M*** precessions show a strong dependence on the polarization direction of linearly polarized pump pulses of 400 nm. In contrast, we can barely observe any ***M*** precession using circularly polarized pump pulses, which indicates that the inverse Faraday effect is negligible. For the case of linear pump polarization, a phenomenological model is introduced, based on the modulation of ***M*** via a modulation of fourth-rank susceptibility tensors by a laser pulse. This allows one to distinguish the contributions of the inverse Cotton-Mouton effect (ICME) from those of the photoinduced magnetic anisotropy (PMA). Using the formula derived from the phenomenological model, we perform the fitting of the polarization-direction-dependent precession phase and amplitude in (100)- and (111)-oriented YIG films. The fitting results reveal that the ***M***-precession excitation originates from a combination effect of ICME and PMA, but the ICME plays the dominant role.

DOI: 10.1103/PhysRevB.97.224430

I. INTRODUCTION

The demand for magnetic recording devices with increased speed and capacity has intrigued many interests in exploring novel concepts for faster and more energy efficient control of the magnetization (***M***) [1–6]. Ultrafast optical manipulation of ***M*** by femtosecond (fs) laser pulse is a promising way therein. The fs laser pulse has advantages in driving the ***M*** dynamics owing to its short time duration comparable to the timescale of spin-exchange interaction [7]. A wealth of experimental studies has demonstrated fs laser-induced ultrafast demagnetization, coherent spin rotation, and even magnetic phase transition at picosecond (ps) timescale in magnetic materials [8–14]. Nevertheless, the related physics of the ultrafast spin dynamics is still poorly understood and has received great attention [7].

In general, the excitation of a laser pulse on ***M*** can be classified into thermal and nonthermal effects [5–7]. The thermal effect can be described by the phenomenological three-temperature model, in which the pump light is absorbed by the magnetic medium, causing a heat transfer among electrons, lattice, and spins [15,16]. The thermal effect depends on the pump light intensity but has no relation with the pump light polarization. In contrast, the ***M*** dynamics induced by nonthermal effect usually shows strong dependence on the pump light polarization. Nonthermal all-optical coherent manipulation of magnetization has great values for practical application owing to its negligible heat accumulation and high repetition rate [6,17,18], and therefore it has attracted much interest in the recent decade. To date, there are mainly two types of nonthermal effect reported in the literature. One is the photoinduced magnetic anisotropy (PMA) involved with the direct absorption of pump light photons [6,19,20] and the other is the optomagnetic effect without photon absorption [19]. Photoexcited electron transfer between different ions is normally considered as the origin of the PMA effect [21–23], whereas the mechanism of the optomagnetic effect is based on the impulsive stimulated Raman scattering (ISRS) [5,7,18,24,25].The optomagnetic effect can be further classified into the inverse Faraday effect (IFE) and the inverse Cotton-Mouton effect (ICME), which are induced by circularly and linearly polarized light, respectively [7,26–28].

The nonthermal effect on the ultrafast ***M*** dynamics has been studied by time-resolved magneto-optical Kerr effect (TRMOKE) in different materials like orthoferrites [5,18,29,30], garnets [23,31], antiferromagnets [32,33], and III-V magnetic semiconductors [6,34–36]. Garnet has large magneto-optical effect, low optical absorption, and small damping of magnetic excitation, so it is considered as an ideal material for use in ultrafast magnetic recording [37,38]. Recently, laser-induced ***M*** precessions have been observed in various iron garnets, which are either doped with elements of different groups (Co, Si, Bi) [31,39–41] or introduced with some impurities (Pb) [42]. The dopants may greatly enhance the magneto-optical response and also the magnetic anisotropy [43,44]. Consequently, in most of the doped garnets excited by fs laser pulses, the IFE and PMA were found

*hbzhao@fudan.edu.cn

to be the dominating effects. For example, both IFE and PMA were considered as the origin of the $\boldsymbol{M}$ precession in $Lu_{1.69}Y_{0.65}Bi_{0.66}Fe_{3.85}Ga_{1.15}O_{12}$ [23,31] and $Bi_{0.3}Y_{2.7}Fe_5O_{12}$ [45]. In contrast, PMA mainly accounted for the $\boldsymbol{M}$-precession excitation in $Y_2CaFe_{3.9}Co_{0.1}GeO_{12}$ [46]. A combination effect of PMA and ICME was revealed to be responsible for the excitation of $\boldsymbol{M}$ precession in $Gd_{4/3}Yb_{2/3}BiFe_5O_{12}$ [39,40]. To our best knowledge, there is no report yet on the dominating role of the ICME for driving the $\boldsymbol{M}$ precessions in garnets. In fact, the ICME has advantage over the PMA effect regarding to the large driving torque and short timescale for controlling $\boldsymbol{M}$. In addition, it may be used to continuously tune the driving-field direction by simply rotating the light polarization, which is beyond the capability of the IFE.

Although the pump polarization dependence of the $\boldsymbol{M}$ dynamics represents a critical evidence to define the nonthermal effect, the specific analysis of such a dependence to identify the real mechanism is not straightforward. In particular, both PMA and ICME have a similar dependence on the polarization direction of the linearly polarized pump light. So in order to distinguish these two effects, their relaxation times have to be considered. Typically, PMA is displacive, but ISRS is impulsive. Actually, for an accurate description, the crystal-field theory, spin-orbit coupling and exchange should be considered, yielding a very complex theory [47]. Alternatively, a phenomenological model using the effective magnetic fields derived from the modulated Hamiltonian by laser in combination with the Landau-Lifshitz (LL) equation has been developed to describe the laser-induced $\boldsymbol{M}$ dynamics [25,39,48,49]. Nevertheless, the model involves many parameters, so the detailed analysis of the $\boldsymbol{M}$ dynamics conducted in one single sample might lead to uncertainty [39].

In this paper, we report studies on the ultrafast laser-induced $\boldsymbol{M}$ precessions in undoped yttrium iron garnet films epitaxially grown on gadolinium gallium garnet (GGG) substrates with (100) and (111) orientations. We perform the simultaneous analysis of polarization-dependent $\boldsymbol{M}$ precessions in two samples using the macroscopic phenomenological model. The analysis reveals that the $\boldsymbol{M}$-precession excitation is due to a combination effect of ICME and PMA, but the ICME is dominant. The rest of this paper is organized as follows. In Sec. II, we give the model for laser-induced $\boldsymbol{M}$ dynamics. In Sec. III, the experimental details are introduced. In Sec. IV, we present the TRMOKE results in YIG (100) and (111) films excited by fs laser, and apply the model in Sec. II to analyze the polarization dependence of laser-induced $\boldsymbol{M}$ precessions, and finally we come to the conclusion in Sec. V.

II. MODEL FOR LASER-INDUCED MAGNETIZATION DYNAMICS

A. Nonthermal photomagnetic effects

In this part, we first illustrate two different types of nonthermal photomagnetic effect, which is classified by whether it depends on the absorption of photons [7]. Each of them acts on the medium by creating transient magnetic field ($\boldsymbol{H}_t$), thereby causing $\boldsymbol{M}$ to rotate. A unified macroscopic model is then introduced to describe the photomagnetic effect.

The first category, optomagnetic effect associated with the inverse magneto-optical effect, including the IFE and the ICME, originates from the ISRS without direct absorption of photons [49–51]. The optomagnetic effect only occurs during the light illumination, so the $\boldsymbol{H}_t$ has the same duration as the pump laser pulse. The IFE manifests as a strong $\boldsymbol{H}_{\mathrm{IFE}}$ induced by circularly polarized pump light, whereas the ICME yields strong $\boldsymbol{H}_{\mathrm{ICME}}$ caused by linearly polarized light. For IFE, circularly polarized light with inverse helicities ($\sigma^{\pm}$) will lead to opposite $\boldsymbol{H}_{\mathrm{IFE}}$ along the wave vector of the light [5,7], while for ICME, linearly polarized light with different polarization planes will change the direction and amplitude of $\boldsymbol{H}_{\mathrm{ICME}}$. Such a polarization dependence can be understood from the macroscopic model we introduced below. As a nonthermal process, either IFE or ICME represents an efficient way to excite a magnetic system at an ultrafast timescale much shorter than the spin-precession period.

The second category known as the PMA effect depends on the absorption of photons. Such an effect is often observed in garnets containing dopants artificially introduced (e.g., Co) [52] or impurities (e.g., Pb) [42] inevitably produced in the growth process. For the former, the dopants directly modify the magnetic anisotropy. For the latter, impurities (or defects) serve as donators or acceptors in the crystal [53], thus the ions in the vicinity will change valence to maintain charge neutrality. These dopants or impurities result in orientationally nonequivalent sites for charge transfer between magnetic ions upon laser excitation, which is equivalent to the photoinduced redistribution of anisotropic ions. The excitation probabilities of nonequivalent sites depend on the light polarization, while the overall absorption remains unchanged. Therefore, the PMA effect yields a long-lived anisotropy field $\boldsymbol{H}_{\mathrm{PMA}}$ depending on the pump light polarization.

Despite different microscopic origins of the photoinduced $\boldsymbol{H}_t$, a phenomenological macroscopic model can be used to describe the above photomagnetic effects. When a magnetic medium is excited by an intensive laser, it undergoes a permittivity modulation of $\delta\varepsilon_{ij}$, which depends on $\boldsymbol{M}$ of the medium. The Hamiltonian describing such a light-medium interaction in a cubic magnet can be written as [24,54,55]

$$\mathcal{H}_{\mathrm{int}} = -\frac{\delta\varepsilon_{ij}}{16\pi}\mathcal{E}_i(t)\mathcal{E}_j^*(t), \tag{1}$$

where $\mathcal{E}_i(t)$ denotes the time-dependent electric-field strength of light, and $\delta\varepsilon_{ij}$ is described as [56]

$$\delta\varepsilon_{ij} = ik_{ijl}\delta M_l + 2g_{ijkl}M_k\delta M_l. \tag{2}$$

Here, k_{ijk} and g_{ijkl} represent the third-rank axial and fourth-rank polar susceptibility tensors, respectively, which can be determined from the crystal point group discussed in details below, and δM_l represents the $\boldsymbol{M}$ modification along the l direction. The light-induced transient magnetic field can thus be written as [57]

$$\boldsymbol{H}_t = -\frac{\partial\mathcal{H}_{\mathrm{int}}}{\partial\delta\boldsymbol{M}}. \tag{3}$$

On the right side of Eq. (2), the first term describes the linear effect of $\boldsymbol{M}$ on the permittivity, which is related to the Faraday effect, and the second term represents a quadratic dependence on $\boldsymbol{M}$ (only the first order of $\delta\boldsymbol{M}$ is retained), which

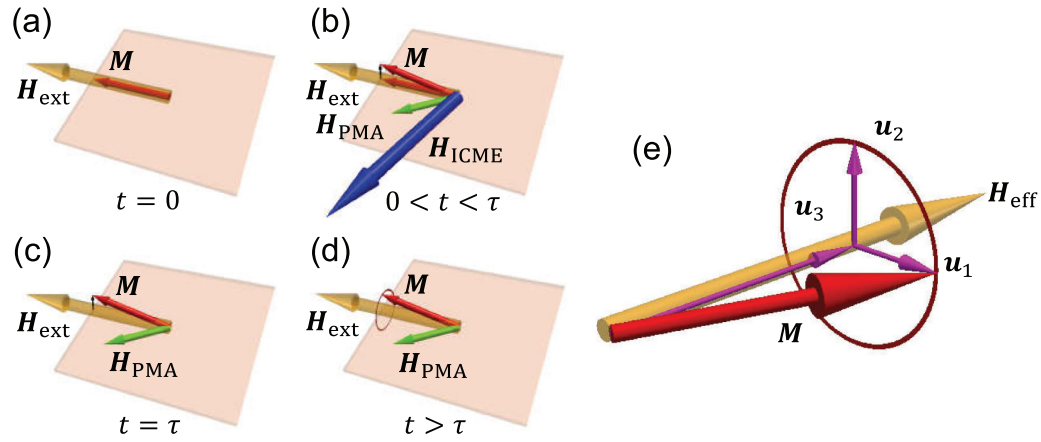

FIG. 1. Schematic illustration of the $\boldsymbol{M}$ precession excited by $\boldsymbol{H}_{\mathrm{ICME}}$ and $\boldsymbol{H}_{\mathrm{PMA}}$. (a)–(d) Behavior of $\boldsymbol{M}$ at different timescales. Here, τ denotes the duration of the pump pulse. (e) Three perpendicular $\boldsymbol{M}$ components during the precession period. Here, we make illustration using in-plane $\boldsymbol{H}_{\mathrm{ICME}}$ and $\boldsymbol{H}_{\mathrm{PMA}}$. Actually, for YIG (100), both fields are mainly within the film plane, but for YIG (111), both fields have large out-of-plane components comparable to the in-plane components as discussed in Sec. IV.

corresponds to the Cotton-Mouton effect. Applying Eq. (1) and Eq. (2) to Eq. (3), we obtain the transient IFE and ICME fields as

$$(\boldsymbol{H}_{\mathrm{IFE}})_l^{\sigma^{\pm}} = -\frac{\partial \mathcal{H}_{\mathrm{int}}^{\sigma^{\pm}}}{\partial \delta \boldsymbol{M}_l} = \begin{cases} \pm\frac{1}{16\pi} k_{ijl}\mathcal{E}_i\mathcal{E}_j^*, & 0 < t \leqslant \tau \\ 0, & t > \tau, \end{cases} \tag{4}$$

$$(\boldsymbol{H}_{\mathrm{ICME}})_l = -\frac{\partial \mathcal{H}_{\mathrm{int}}}{\partial \delta \boldsymbol{M}_l} = \begin{cases} \frac{1}{8\pi} g_{ijkl} M_k \mathcal{E}_i\mathcal{E}_j^*, & 0 < t \leqslant \tau \\ 0, & t > \tau, \end{cases} \tag{5}$$

where τ denotes the time duration of laser pulses.

For PMA, although the electric field vanishes for $t > \tau$, the field-induced charge transfer and the resultant anisotropy field usually persist much longer and exceed the period of spin precession. In this case, the PMA relaxation impact on the spin dynamics can be neglected. Therefore, we consider the Hamiltonian as a step function, and then the transient anisotropy field is written as [44,58]

$$(\boldsymbol{H}_{\mathrm{PMA}})_l = \frac{1}{8\pi} a_{ijkl} M_k \mathcal{E}_i\mathcal{E}_j^*,\ t \leqslant T, \tag{6}$$

Here, T is the time duration of the PMA field, and a_{ijkl} denotes the fourth-rank polar susceptibility tensor, possessing the same form as g_{ijkl}.

B. Magnetization dynamics

In this part, we briefly describe the $\boldsymbol{M}$ dynamics driven by the photomagnetic field $\boldsymbol{H}_{\mathrm{t}}$. When $\boldsymbol{M}$ is not parallel to the effective magnetic field $\boldsymbol{H}_{\mathrm{eff}}$, it will experience a torque perpendicular to the plane formed by $\boldsymbol{M}$ and $\boldsymbol{H}_{\mathrm{eff}}$. Thus, $\boldsymbol{M}$ will precess around $\boldsymbol{H}_{\mathrm{eff}}$. This process is described by the LL equation [59,60]:

$$\mathrm{d}\boldsymbol{M}/\mathrm{d}t = -\gamma(\boldsymbol{M} \times \boldsymbol{H}_{\mathrm{eff}}), \tag{7}$$

where γ is the gyromagnetic ratio. The $\boldsymbol{H}_{\mathrm{eff}}$ is composed of the externally applied field $\boldsymbol{H}_{\mathrm{ext}}$, the anisotropy field $\boldsymbol{H}_{\mathrm{a}}$, and the demagnetization field $\boldsymbol{H}_{\mathrm{d}}$. The interaction between light and medium will generate a transient field $\boldsymbol{H}_{\mathrm{t}}$, which may deviate from $\boldsymbol{M}$, and so upon laser excitation, $\boldsymbol{M}$ will start to rotate around a new $\boldsymbol{H}_{\mathrm{eff}}$. As an example, we consider a combined effect of ICME and PMA on the $\boldsymbol{M}$ dynamics in a thin YIG film. The behavior of $\boldsymbol{M}$ at different timescales is illustrated in Fig. 1 for the case of in-plane fields $\boldsymbol{H}_{\mathrm{ext}}$ implemented in the TRMOKE experiments of this work. Before the laser pulse reaches the sample ($t < 0$), $\boldsymbol{M}$ is nearly aligned along $\boldsymbol{H}_{\mathrm{ext}}$ if $\boldsymbol{H}_{\mathrm{a}}$ is much smaller than $\boldsymbol{H}_{\mathrm{ext}}$. During the laser pulse excitation ($0 < t \leqslant \tau$), ICME causes an impulsive field $\boldsymbol{H}_{\mathrm{ICME}}$, which is strong enough to rapidly tilt $\boldsymbol{M}$, and meanwhile PMA generates $\boldsymbol{H}_{\mathrm{PMA}}$. Normally $\boldsymbol{H}_{\mathrm{PMA}}$ is much weaker than $\boldsymbol{H}_{\mathrm{ICME}}$, so we assume that $\boldsymbol{H}_{\mathrm{PMA}}$ can be neglected during this period. The correctness of this assumption is proved later in Results and Discussion. After the pump excitation finishes ($t > \tau$), $\boldsymbol{H}_{\mathrm{ICME}}$ vanishes, whereas $\boldsymbol{H}_{\mathrm{PMA}}$ still remains, as the ion redistribution caused by the laser pulse is displacive. Hence, right after the vanishing of the pump pulse, $\boldsymbol{M}$ becomes $\boldsymbol{M}(t = \tau) = \boldsymbol{M}_0(\mathrm{t} = 0) - \tau\gamma(\boldsymbol{M}_0 \times \boldsymbol{H}_{\mathrm{ICME}})$, which will then precess around $\boldsymbol{H}_{\mathrm{eff}} = \boldsymbol{H}_{\mathrm{ext}} + \boldsymbol{H}_{\mathrm{a}} + \boldsymbol{H}_{\mathrm{d}} + \boldsymbol{H}_{\mathrm{PMA}}$. This scenario is also applicable for cases when IFE generates a strong impulsive field, $\boldsymbol{H}_{\mathrm{IFE}}$.

III. EXPERIMENT

We studied two undoped $Y_3Fe_5O_{12}$ films ($d = 30$ nm) epitaxially grown on the GGG substrate (100) and (111) by pulsed laser deposition. Although the two films are nominal pure YIG, the oxygen vacancies/defects during growth were unavoidable, thus resulting in some Fe^{2+} ions. Both samples are monocrystalline as determined from the reflective high-energy electron diffraction, and their Curie temperature T_c is ~550 K. The saturated magnetization M_s is ~140 emu/cm^3 and the in-plane magnetic hysteresis loops measured by a superconducting quantum interference device (SQUID) are shown in Fig. 2. The hysteresis loops are nearly square-shaped and quite narrow, so the magnetocrystalline anisotropy is very small.

The ultrafast laser-induced $\boldsymbol{M}$ dynamics of the two samples were studied using the TRMOKE technique. The schematic experimental geometry is shown in Fig. 3. The ultrafast laser with a pulse width of ~100 fs, a repetition rate of 1 kHz, and

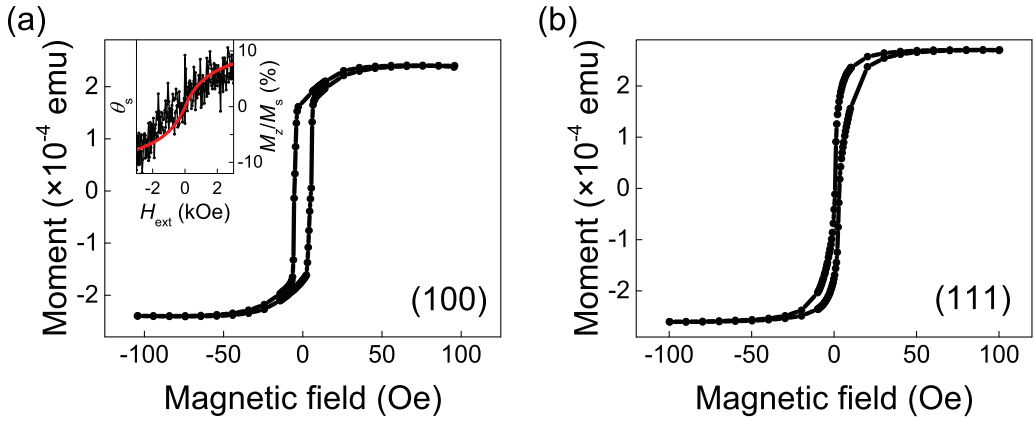

FIG. 2. Magnetic hysteresis loops measured by SQUID for (a) YIG (100) with $\boldsymbol{H}_{\text{ext}} \parallel [010]$, and (b) YIG (111) with $H_{\text{ext}} \parallel [01\bar{1}]$. The inset of Fig. 1(a) shows static MOKE signals and calculated out-of-plane M_z (solid line) for $\boldsymbol{H}_{\text{ext}}$ at ~6° with respect to the sample plane.

a central wavelength of 800 nm emitted from a Ti: sapphire amplifier system was split into two beams for use as the pump and probe. We used a 400-nm pulse generated by a beta barium borate crystal for the pump incident perpendicularly and an 800-nm pulse for the probe at an incident angle of ~45°. The use of different wavelengths of the pump and probe helped avoid scattering signal in the measurements. The pump fluence was as low as ~3 mJ/cm^2, much smaller than that used for excitation of garnets in the literature. The polarization rotation (θ_P) of the reflected probe pulses was detected by a balanced detector in combination of a half-wave retarder and a Wollaston prism. A vector magnet was used to provide magnetic fields $\boldsymbol{H}_{\text{ext}}$ along arbitrary directions in the sample plane. We only detected the out-of-plane $\boldsymbol{M}$ component (M_z) because no Kerr rotation signals from the in-plane $\boldsymbol{M}$ component could be resolved in the static MOKE measurements using the in-plane $\boldsymbol{H}_{\text{ext}}$. The inset of Fig. 2(a) shows the static MOKE signal (θ_s) measured with $\boldsymbol{H}_{\text{ext}}$ applied at ~6° with respect to the

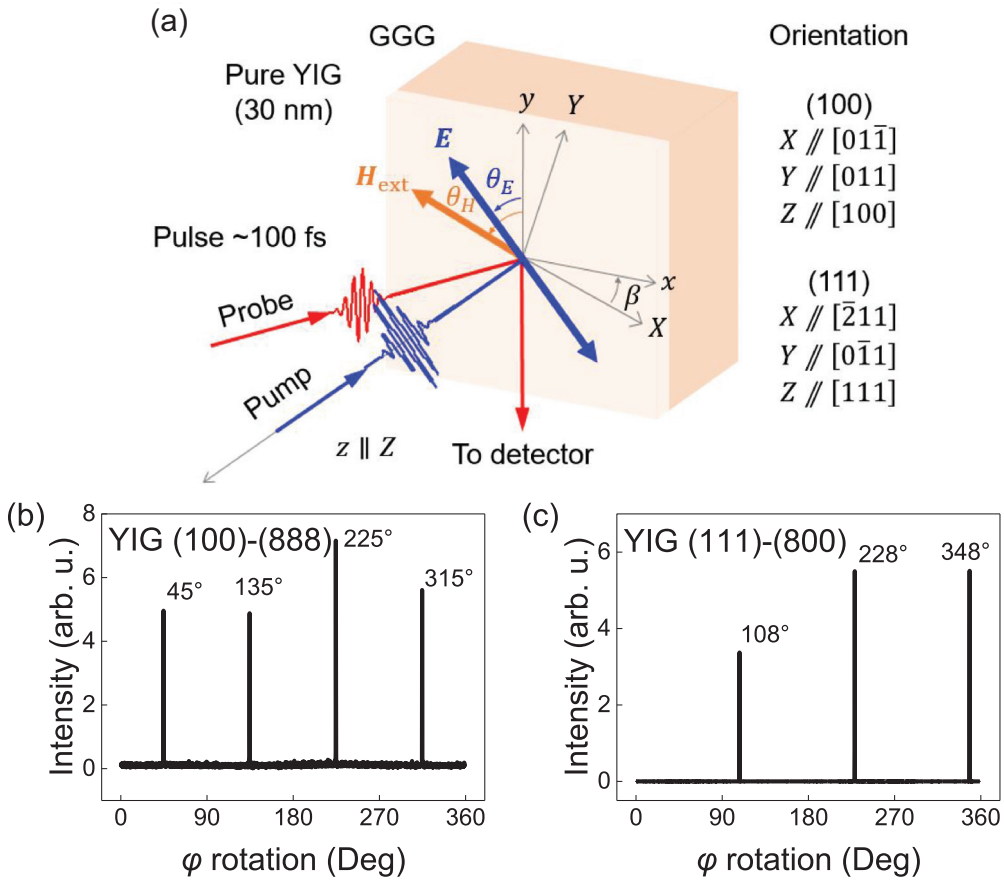

FIG. 3. (a) Experimental geometry in $\{x,y,z\}$ and $\{X, Y, Z\}$ coordinate systems, (b) XRD φ-scan for YIG (100) with first peak at $\varphi = 45°$, and (c) XRD φ-scan for YIG (111) with first peak at $\varphi = 108°$.

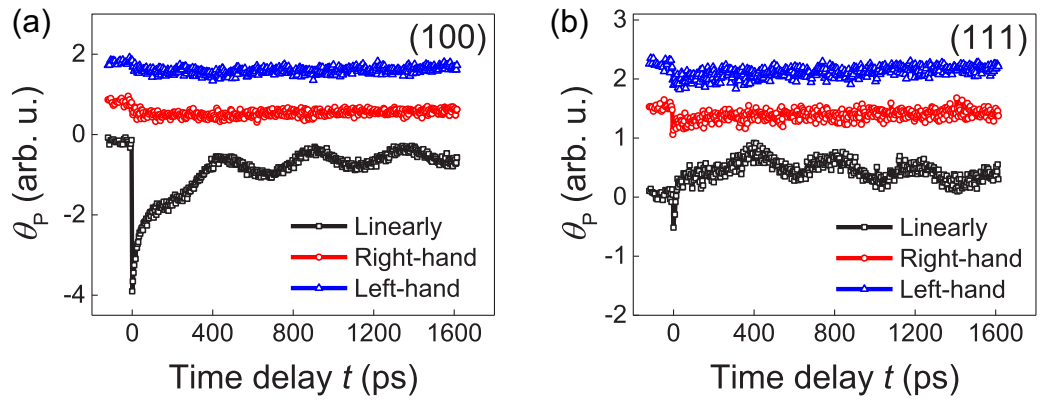

FIG. 4. Polarization rotation θ_P of the probe beam as a function of time delay in (a) YIG (100) and (b) YIG (111) excited by pump pulses with linear, and right- and left-circular polarizations.

film plane of YIG (100). We note that there is no abrupt θ_s jump corresponding to the in-plane $\boldsymbol{M}$ reversal close to zero field. However, the θ_s shows a gradual change with the $\boldsymbol{H}_{\rm ext}$ sweeping between ± 3 kOe. Such a MOKE response is caused by the M_z which enhances with the increasing $\boldsymbol{H}_{\rm ext}$. The solid curve represents the ratio of M_z versus M_s determined by $\boldsymbol{H}_{\rm ext}$ and $\boldsymbol{H}_{\rm d}$. Actually, the MOKE response from the M_z was also confirmed from the measured field orientation-dependent $\boldsymbol{M}$ dynamics as discussed later.

For quantitative analysis of the $\boldsymbol{M}$ dynamics using the macroscopic model, we define two sets of coordinate systems. One is $\{x,y,z\}$ with x and y along the sample edges and z perpendicular to the sample surface. The other is $\{X, Y, Z\}$ with X and Y along the certain in-plane crystallographic orientations and Z normal to the sample surface. We determined the in-plane crystal orientations by x-ray diffraction (XRD) φ-scan as shown in Figs. 3(b) and 3(c). In YIG (100) as an example, the incident x ray was set at the diffraction angle of the crystal face (888), and the sample was tilted to lay the crystal face (888) in the horizontal plane. We then rotated the sample around its normal to perform the XRD φ-scan. The first peak position appears at $\varphi = 45^\circ$, which corresponds to the angle of the intersection of the crystal faces (100) and (888) ($[01\bar{1}]$ or [011]) with respect to the sample edge of the x axis along [010]. The measured crystal orientations of YIG (100) and YIG (111) films in the $\{X, Y, Z\}$ coordinate system for use in the TRMOKE measurements are listed in Fig. 3(a). Here, θ_E and θ_H denote the angle of the laser electric-field $\boldsymbol{E}$ and magnetic-field $\boldsymbol{H}_{\rm ext}$ with respect to the y axis, respectively. In the real TRMOKE measurements, a small magnetic-field component along the z direction may exist and we define it as $hH_{\rm ext}$, where $h \ll 1$. β denotes the angle of the X axis with respect to the x axis, e.g., 45° for YIG (100) and 30° for YIG (111). Note that all the angles are defined by counterclockwise rotation. We also define $\theta_1 = \theta_H + \beta$ and $\theta_2 = \theta_E + \beta$ for calculations in the $\{X, Y, Z\}$ coordinate system.

IV. RESULTS AND DISCUSSION

In this section, we first show the TRMOKE results of YIG (100) for different pump polarization and $\boldsymbol{H}_{\rm ext}$. Then, analytical expressions of the precession phase and amplitude as a function of the polarization direction θ_E are given using the model in Sec. II. Following that, we conduct a fit of the θ_E-dependent precession data using the analytical expressions to obtain the fourth-rank susceptibility parameters for calculation of $\boldsymbol{H}_{\rm t}$. The calculated $\boldsymbol{H}_{\rm t}$ enables us to distinguish the contributions of ICME and PMA to the $\boldsymbol{M}$-precession excitation. In addition, we analyze the θ_E-dependent nonoscillating signals in the TRMOKE results. Finally, we show the TRMOKE results in YIG (111) and repeat the analysis. It is important to note that we used the same fourth-rank susceptibility parameters for both samples.

A. Comparison of circularly and linearly polarized light excitation

Figure 4 shows the polarization rotation ($\theta_{\rm P}$) as a function of the time delay (t) in YIG (100) and YIG (111) films excited by ultrafast laser pulses of right-circular, left-circular, and linear polarizations. All these curves were obtained at the same field of $H_{\rm ext} = 0.3$ kOe, and $\theta_H = 10^\circ$. We note that linearly polarized pump pulses can trigger in both samples the $\boldsymbol{M}$ precessions, manifested as the periodic oscillations in $\theta_{\rm P}(t)$, whereas the circularly polarized pulses can hardly excite any precession. Actually, we could barely observe any oscillations under various $\boldsymbol{H}_{\rm ext}$ for circularly polarized laser excitation. Such an apparent polarization dependence of spin-precession excitation is consistent with the excitation mechanism of a nonthermal effect. Moreover, we can exclude the $\boldsymbol{H}_{\rm IFE}$ as the driving force of spin precessions since the IFE is just produced by the circularly polarized light. In Eq. (4) and Eq. (5), k and gM determine the strength of $\boldsymbol{H}_{\rm IFE}$ and $\boldsymbol{H}_{\rm ICME}$, so we believe that k is very small compared to gM. In addition to the $\boldsymbol{M}$ precession, a decayed nonoscillating signal appears in both samples, which will be discussed later.

B. TRMOKE for different θ_E and $H_{\rm ext}$ in YIG (100)

We then measured the dependence of $\theta_{\rm P}(t)$ on the polarization direction (θ_E) of the linearly polarized pump laser, as shown in Fig. 5. We fitted each $\theta_{\rm P}(t)$ curve with the function of

$$\theta_{\rm P}(t) = A\exp(-Bt)\sin(2\pi f t + C) + A_0\exp(-t/t_0) + A_1\exp(-t/t_1) \quad (8)$$

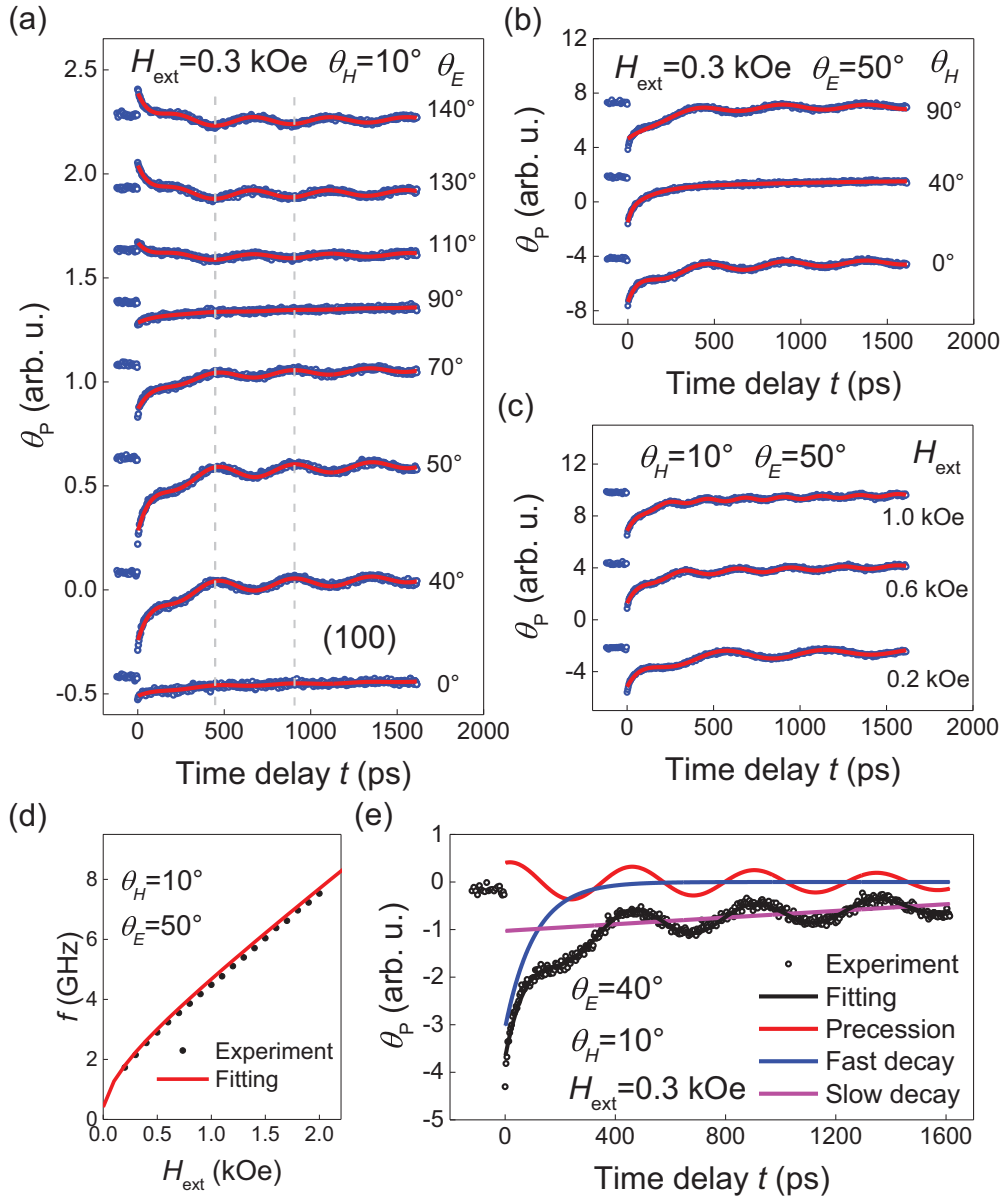

FIG. 5. $\theta_P(t)$ for different (a) polarization direction θ_E, (b) field orientation θ_H, and (c) field strength H_{ext} in YIG (100). Solid lines represent fittings to Eq. (8). (d) The field strength H_{ext} dependence of precession frequency f. The solid line is a fitting using the Kittel formula. (e) An example of the three components in $\theta_P(t)$ obtained from the fitting to Eq. (8).

where the first term represents the damped oscillations corresponding to the $\boldsymbol{M}$ precession, and the second and third terms represent the fast-decay and slow-decay nonoscillating signals, respectively. An example of the fitting curve with three components is shown in Fig. 5(e). From the fitting results, we obtained the precession amplitude A and phase C as a function of θ_E shown in Fig. 6, and the amplitude A_0 and A_1 as a function of θ_E shown in Fig. 7.

To confirm that the oscillations originate from the $\boldsymbol{M}$ precession, we also measured $\theta_P(t)$ for different field orientation (θ_H) and strength (H_{ext}), as shown in Figs. 5(b) and 5(c), and thereby we obtained the field-strength dependence of precession frequency f as shown in Fig. 5(d). A reasonable good fit of the f versus H_{ext} using the Kittel formula (details are in Appendix A) was achieved. The H_a determined from the fit is as small as ~10 Oe, in accordance with the hysteresis loop. Because H_a is small, f shows no apparent θ_H dependence. In addition, we note from Fig. 5(b) that the precession amplitude A is nearly identical for $\boldsymbol{H}_{ext}$ along the x axis ($\theta_H = 90°$) and y axis ($\theta_H = 90°$). This result confirms that the oscillating Kerr signals are caused by the polar M_z component because there is no precessing longitudinal M_x component for $\theta_H = 90°$ [61]. The nonoscillating signals show no field dependence, and thus we rule out the MOKE contributions to them.

The observation of strong dependence of precession amplitude A and phase C on θ_E confirms that the excitation mechanism is due to the nonthermal effect. In order to further distinguish the contributions from ICME and PMA to the $\boldsymbol{M}$-precession excitation, we conduct in the next part a detailed analysis of θ_E-dependent A and C using the model developed

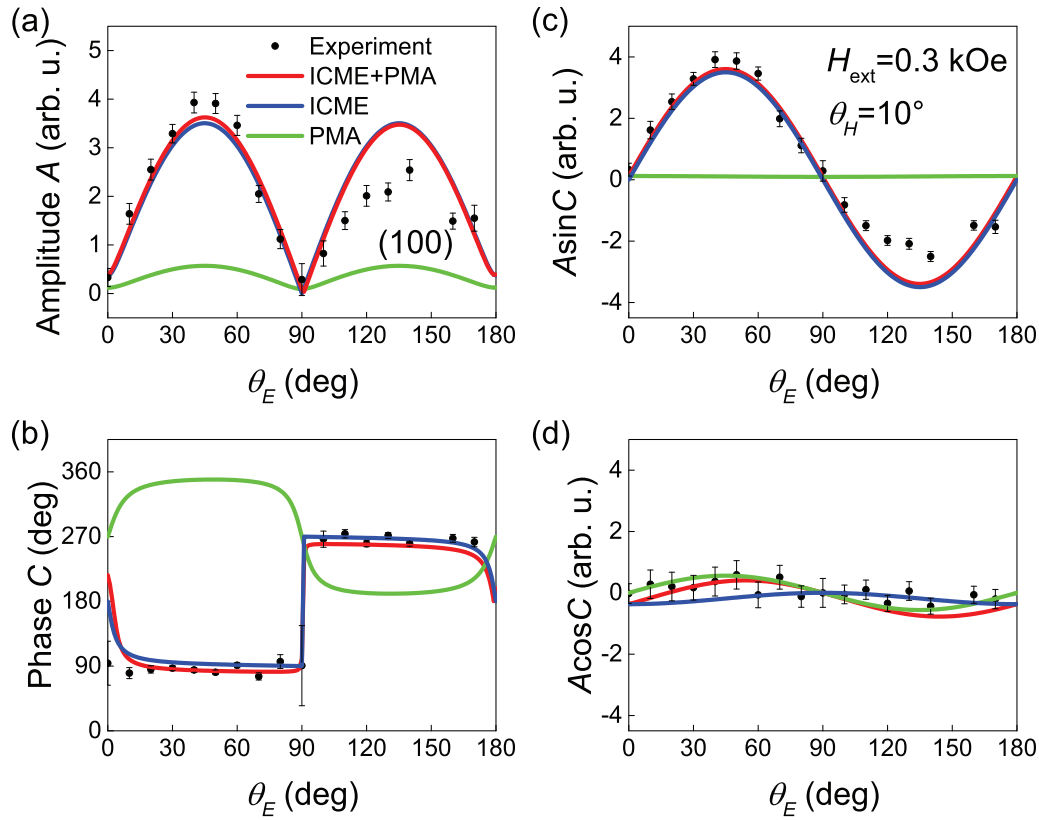

FIG. 6. Polarization direction (θ_E) dependence of (a) amplitude A, (b) phase C, (c) $A \sin C$, and (d) $A \cos C$ of the $\boldsymbol{M}$ precession in YIG (100). The red lines are fitting curves considering a combination of ICME and PMA effects, and the blue and green lines represent the separate contributions of the ICME and PMA, respectively.

in Sec. II. We will also discuss the origin of the nonoscillating signals.

C. Analysis of θ_E dependence of polarization rotation in YIG (100)

In Sec. II, we have presented a phenomenological model to describe the $\boldsymbol{M}$ precession. Now, we will apply it to identify the underlying mechanism, ICME or PMA or a combination of them.

For convenience of analyzing the $\boldsymbol{M}$ precession observed in the time domain, we adopted the strategies developed by Yoshimine *et al.* [39]. $\boldsymbol{M}(t = \tau)$ is decomposed into two vectors of $\boldsymbol{u}_1$ and $\boldsymbol{u}_3$, which represent the components normal and parallel to $\boldsymbol{H}_{\text{eff}}$, respectively [see Fig. 1(e)]. Another vector $\boldsymbol{u}_2$, satisfying the condition of $|\boldsymbol{u}_1| = |\boldsymbol{u}_2|$, $\boldsymbol{u}_2 \perp \boldsymbol{H}_{\text{eff}}$, and $\boldsymbol{u}_2 \perp \boldsymbol{M}(t = \tau)$, is also introduced. After neglecting the damping, the $\boldsymbol{M}$ precession can then be described as follows:

$$\boldsymbol{M}(t > \tau) = \boldsymbol{u}_1 \cos 2\pi f t + \boldsymbol{u}_2 \sin 2\pi f t + \boldsymbol{u}_3. \quad (9)$$

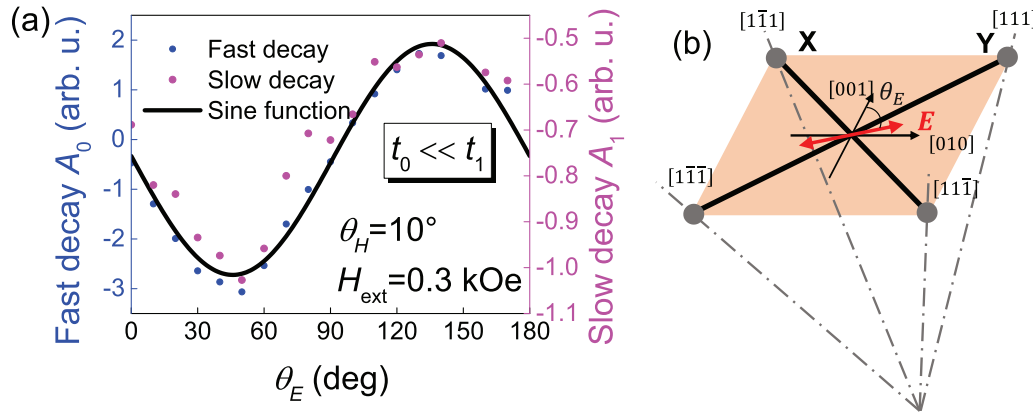

FIG. 7. (a) Polarization direction (θ_E) dependence of the amplitudes of fast-decay and slow-decay nonoscillating signals in YIG (100). The solid line represents a fitting by the sinusoidal function. (b) Illustration of the orientationally inequivalent octahedral Fe sites in YIG (100).

Here,

$$\boldsymbol{u}_1 = \boldsymbol{M}(t=\tau) - \frac{\boldsymbol{M}(t=\tau)\cdot\boldsymbol{H}_{\text{eff}}}{|\boldsymbol{H}_{\text{eff}}|^2}\boldsymbol{H}_{\text{eff}}, \tag{10a}$$

$$\boldsymbol{u}_2 = -\frac{\boldsymbol{M}(t=\tau)\times\boldsymbol{H}_{\text{eff}}}{|\boldsymbol{H}_{\text{eff}}|}, \tag{10b}$$

$$\boldsymbol{u}_3 = \frac{\boldsymbol{M}(t=\tau)\cdot\boldsymbol{H}_{\text{eff}}}{|\boldsymbol{H}_{\text{eff}}|^2}\boldsymbol{H}_{\text{eff}}. \tag{10c}$$

Let us expand the first term on the right side of Eq. (8), and so it becomes

$$\phi_{\text{K}}(t) = \exp(-Bt)[A\sin C\cos 2\pi f t + A\cos C\sin 2\pi f t]. \tag{11}$$

The Kerr rotation of the probe pulses is proportional to the M_z component

$$\phi_{\text{K}} = K M_z, \tag{12}$$

and therefore, after neglecting the decay of the $\boldsymbol{M}$ precession, we end up with

$$K(\boldsymbol{u}_1)_z = A\sin C, \tag{13a}$$

$$K(\boldsymbol{u}_2)_z = A\cos C. \tag{13b}$$

To determine $\boldsymbol{M}(t=\tau)$ and $\boldsymbol{H}_{\text{eff}}$, we need to first establish the fourth-rank polar tensor $\boldsymbol{g}$ and $\boldsymbol{a}$ from the crystal point group and the experimental geometry. According to the lattice structure, crystal point group of $m3m$ is given for the bulk YIG. Here we neglect the surface-induced symmetry breaking. Compared to the surface region ($\sim$ 1 nm), 30 nm may be thick enough for the sample to manifest the bulk effect instead of the surface effect. For YIG (100), the X-, Y-, and Z axes represent $[01\bar{1}]$, [011], and [100], respectively, and the x-, y-, and z-axes represent [010], [001], and [100], respectively. By considering the experimental geometry, only three independent nonzero components of $\boldsymbol{g}$ (same for $\boldsymbol{a}$) remain in the $\{x, y, z\}$ coordinate system as follows (see detailed information in Appendix B):

$$g_{xxxx} = g_{yyyy} = g_1, \tag{14a}$$

$$g_{xxyy} = g_{yyxx} = g_{xxzz} = g_{yyzz} = g_2, \tag{14b}$$

$$g_{xyxy} = g_{yxxy} = g_{xyyx} = g_{yxyx} = g_3. \tag{14c}$$

After substituting Eq. (14) into Eq. (5) and Eq. (6) and neglecting the second-order small terms (e.g., h^2 terms), we obtain the expressions for $\boldsymbol{H}_{\text{ICME}}$ ($\boldsymbol{H}_{\text{PMA}}$ can be obtained by replacing $\boldsymbol{g}$ with $\boldsymbol{a}$):

$$(\boldsymbol{H}_{\text{ICME}})_x = \frac{\chi H_{\text{ext}}\mathcal{E}_0^2}{8\pi}\left(\frac{g_1+g_2}{2}\cos\theta_1 + \frac{g_1-g_2}{2}\cos\theta_1\cos 2\theta_2 + g_3\sin\theta_1\sin 2\theta_2\right), \tag{15a}$$

$$(\boldsymbol{H}_{\text{ICME}})_y = \frac{\chi H_{\text{ext}}\mathcal{E}_0^2}{8\pi}\left(\frac{g_1+g_2}{2}\cos\theta_1 - \frac{g_1-g_2}{2}\sin\theta_1\cos 2\theta_2 + g_3\cos\theta_1\sin 2\theta_2\right), \tag{15b}$$

$$(\boldsymbol{H}_{\text{ICME}})_z = \frac{\chi H_{\text{ext}}\mathcal{E}_0^2}{8\pi}(h g_2) \tag{15c}$$

Here, we define $M_0 = \chi H_{\text{ext}}$. So far, we have already obtained all the expressions needed for Eq. (13), which can then be written as

$$A\sin C = K(\boldsymbol{u}_1)_z = K\frac{\chi^2 H_{\text{ext}}\mathcal{E}_0^2}{8\pi}\left[\left(\tau\gamma H_{\text{ext}}\frac{g_1-g_2}{2}\sin 2\theta_1\cos 2\theta_2 - \tau\gamma H_{\text{ext}} g_3\cos 2\theta_1\sin 2\theta_2\right)\right.$$
$$\left. + \left(-\frac{h(a_1-a_2)}{2}\cos 2\theta_1\cos 2\theta_2 - h a_3\sin 2\theta_1\sin 2\theta_2 - h\left(\frac{a_1+3a_2}{2}\right)\right)\right] \tag{16a}$$

$$A\cos C = K(\boldsymbol{u}_2)_z = K\frac{\chi^2 H_{\text{ext}}\mathcal{E}_0^2}{8\pi}\left[\left(h\tau\gamma H_{\text{ext}}\frac{g_1-g_2}{2}\cos 2\theta_1\cos 2\theta_2 + h\tau\gamma H_{\text{ext}} g_3\sin 2\theta_1\sin 2\theta_2 + h\tau\gamma H_{\text{ext}}\left(\frac{g_1-g_2}{2}\right)\right)\right.$$
$$\left. + \left(-\frac{a_1-a_2}{2}\sin 2\theta_1\cos 2\theta_2 + a_3\cos 2\theta_1\sin 2\theta_2\right)\right] \tag{16b}$$

To ensure the accuracy, we also used the coordinate system $\{X, Y, Z\}$ to repeat the above calculations. The two results are identical considering the symmetry rotation operation. Detailed calculations are shown in Appendix C.

Now we can fit our experimental results of θ_E dependence of $A\sin C$ and $A\cos C$ using Eq. (16). We obtained a reasonably good fit for the amplitude A and phase C as shown in Fig. 6. The fitting values of $\boldsymbol{g}$ and $\boldsymbol{a}$ are listed in Appendix D. We then use these values to calculate the separate contributions from ICME and PMA to A and C as shown in Fig. 6. The results indicate that both effects have contributions, but the ICME is dominant for the following reasons.

The ICME has much larger contribution to the amplitude A compared to the PMA. Moreover, the measured phase C is consistent with the phase calculated from the ICME, while it deviates quite a bit from the phase calculated from the PMA. It is important to note that for all θ_E, the phase C is very close to 90° or 270°. Hence, $A\sin C$ is relatively large and determined by ICME, whereas $A\cos C$ resulting from PMA is close to 0 and looks irregular [see Figs. 6(c) and 6(d)]. This phase characteristic indicates that $\boldsymbol{M}$ always has the largest z component when it starts precessional motion around $\boldsymbol{H}_{\text{eff}}$. It can thus be inferred that $\boldsymbol{H}_{\text{ICME}}$ lies mainly in-plane and is large enough to drive $\boldsymbol{M}$ out of the sample plane. Note that the amplitude A

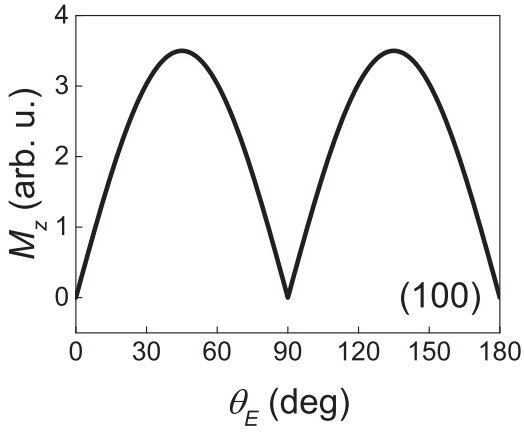

FIG. 8. Calculated z component of $\boldsymbol{M}(t=\tau)$ versus θ_E in YIG (100).

decreases to the minimum when the phase C changes 180° at $\theta_E \approx 90°$, indicating that the direction of $\boldsymbol{H}_{\mathrm{ICME}}$ has switched from one side to the other side of the $\boldsymbol{M}$ according to Eq. (7). This result can be understood from the calculated z component of $\boldsymbol{M}(t=\tau)$ induced by the in-plane $\boldsymbol{H}_{\mathrm{ICME}}$ (see Fig. 8), which almost coincides with the red curve of the amplitude versus θ_E in Fig. 6(a). The out-of-plane $\boldsymbol{H}_{\mathrm{ICME}}$ component does not depend on θ_E [see Eq. (15c)], thus it should not account for the observed θ_E-dependent $\boldsymbol{M}$ precession. Actually, the out-of-plane $\boldsymbol{H}_{\mathrm{ICME}}$ component must be significantly smaller than the in-plane $\boldsymbol{H}_{\mathrm{ICME}}$ component, because otherwise the phase would greatly deviate from 90° or 270°. This reasoning is supported by Eq. (15) and the fitting results shown in Appendix D, which show that g_1 and g_2 are comparable whereas g_3 is much smaller. For the same reason, we can also rule out dominant contributions from the z component of $\boldsymbol{H}_{\mathrm{PMA}}$. Moreover, if the in-plane $\boldsymbol{H}_{\mathrm{PMA}}$ would alternatively dominate the precession excitation, the phase would be close to 0° or 180°, in contrast to the observed results. Actually, we notice that $\boldsymbol{g}$ is approximately five orders of magnitude larger than $\boldsymbol{a}$ (see Appendix D), which also gives strong evidence that ICME is dominant even considering that the duration time of $\boldsymbol{H}_{\mathrm{ICME}}$ is more than three orders of magnitude shorter than the precession period or the duration time of $\boldsymbol{H}_{\mathrm{PMA}}$. This result thus proves the correctness of the assumption that the PMA can be neglected during the laser pulse interaction.

From the fitting parameters, we can calculate the field orientation (θ_H)-dependent precession amplitude. The calculation reveals approximately equal amplitude A for $\theta_H = 0°$ and $\theta_H = 90°$, and almost zero amplitude around $\theta_H = 45°$, in agreement with the measured results in Fig. 5(b). The direct comparison of precession phase is not straightforward because the small out-of-plane field component may change sign for different θ_H. This sign change will result in opposite M_z components and thus induce 180° phase shift in the precession signals. Nevertheless, the measured phase is always close to an integral multiple of 90° for various θ_H as is expected for the ICME.

We have mentioned above that there exist two nonoscillating signals that can be fit by two exponential functions. The fast decay signals have a lifetime of $t_0 \approx 70$ ps, and the slow decay signals exhibit a long lifetime of $t_1 > 1$ ns. The amplitudes A_0 and A_1 versus θ_E satisfy the sinusoidal function as shown in Fig. 7(a). We consider these two signals are from the light-induced birefringence depending on the optically rectified polarization, which is explained in the following. As described in Sec. III, oxygen defects/vacancies were unavoidably introduced in YIG films during the growth. Due to these oxygen vacancies, some octahedrally coordinated Fe^{3+} ions will change their valence and become the strongly anisotropic Fe^{2+} ions, resulting in four magnetically inequivalent distorted octahedral sites [44]. Each octahedral site has a trigonal axis orientated along one of the four body diagonals of the cubic crystallographic cell as shown in Fig. 7(b) [62]. Fe^{2+} ions are randomly distributed among these four sites before light illumination. The linearly polarized laser excites these ions with different probabilities for two orientationally inequivalent X and Y sites, while the total absorption remains unchanged. The probabilities of the electrons that can be excited in X and Y sites are as follows [44]:

$$\sigma_X = \Gamma P[1 + D(1 + \sin 2\theta_E)/2], \tag{17a}$$

$$\sigma_Y = \Gamma P[1 + D(1 - \sin 2\theta_E)/2]. \tag{17b}$$

Here, Γ is a numerical coefficient, P denotes the light intensity, and D is a phenomenological constant. Such an anisotropic excitation leads to a transient electric polarization with various orientations and strengths depending on θ_E. It thus produces the birefringence effect which generates the observed polarization rotation θ_{P} of the probe beam. We speculate that the fast decay component represents the relaxation of the photoexcited high-energy electrons to the lowest-energy excited states, whereas the slow-decay component indicates that the resultant charge redistribution is long-lived. According to Eq. (17), θ_{P} should reach a maximum value with opposite sign for $\theta_E = 45°$ and $\theta_E = 135°$. This behavior is indeed confirmed in Fig. 7(a). Due to the limited time delay in the TRMOKE measurements, we cannot resolve the long-lived θ_{P} induced by the heat from that induced by the charge redistribution. The heat causes a long-lived isotropic signal superimposed onto the anisotropic θ_{P}, yielding an offset of the long-lived θ_{P} above zero. Actually, the anisotropic excitation also accounts for the θ_E-dependent PMA, which is maximal for $\theta_E = (2n+1) \times 45°$, in agreement with the results of the literature [31]. In addition, these long-lived nonoscillating signals indicate that the lifetime of PMA is much longer than the laser pulse duration and is comparable to the $\boldsymbol{M}$-precession period, supporting the model described in Sec. II.

D. TRMOKE for different θ_E and $\boldsymbol{H}_{\mathrm{ext}}$ in YIG (111)

Figure 9 shows $\theta_{\mathrm{P}}(t)$ for different θ_E and $\boldsymbol{H}_{\mathrm{ext}}$ in YIG (111). The $\theta_{\mathrm{P}}(t)$ exhibits strong dependence on θ_E and $\boldsymbol{H}_{\mathrm{ext}}$. We analyzed these results in a similar way as in YIG (100). First, we have confirmed that the oscillation component is due to the $\boldsymbol{M}$ precession from the field-strength dependence of f as shown in Fig. 9(d). The fit of f versus H_{ext} using the Kittel formula reveals very small H_{a} (see Appendix A). The θ_E dependence of the nonoscillating signals in YIG (111) [see Fig. 9(e)] shows similar characteristics as in YIG (100). Both the fast-decay

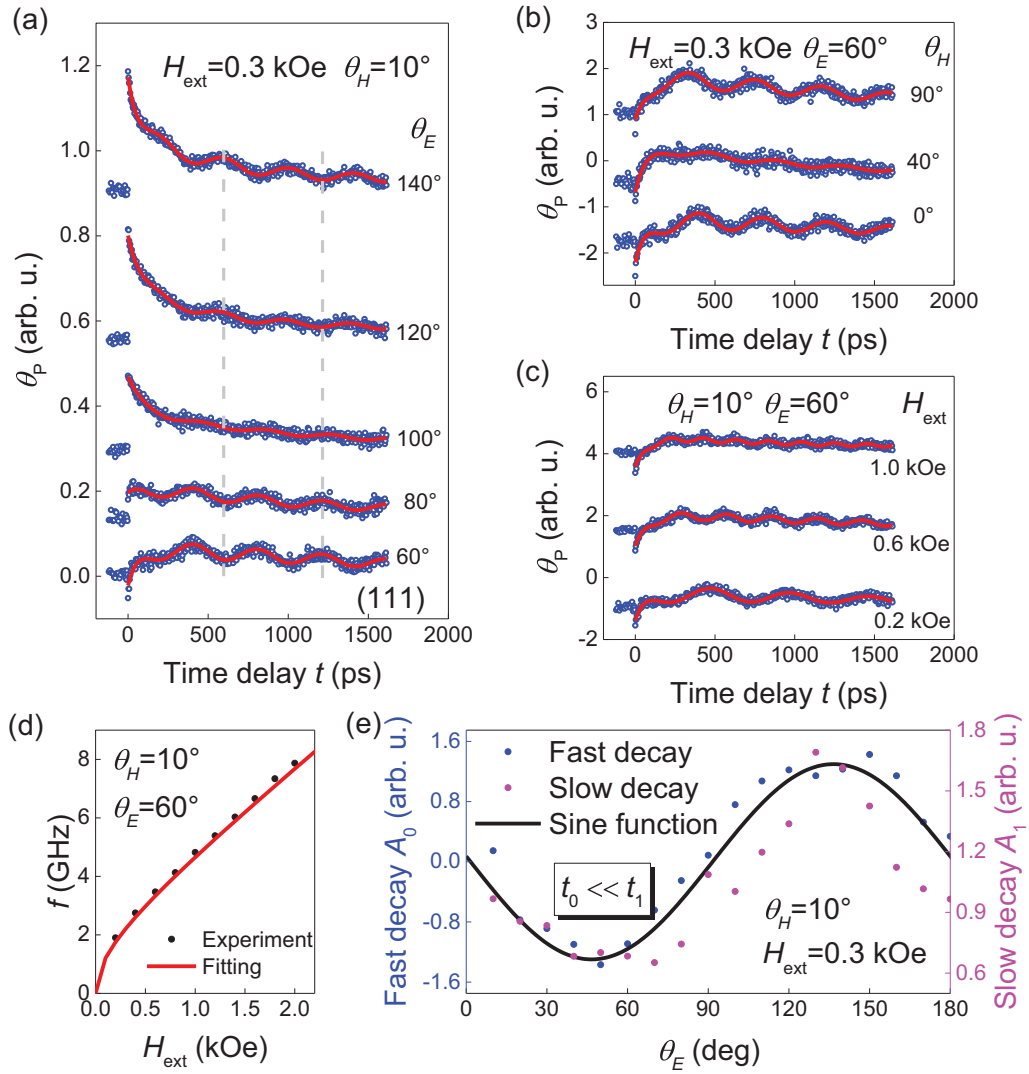

FIG. 9. $\theta_P(t)$ in YIG (111) for different θ_E of linearly polarized pump pulses (a), and different field orientation θ_H (b) and strength H_{ext} (c). The solid lines represent fits to Eq. (8). (d) Field-strength dependence of precession frequency f. The solid line is a fit using the Kittel formula. (e) The amplitudes of nonoscillating signals versus θ_E in YIG (111).

and slow-decay signals versus θ_E are sinusoidal functionlike, representing two relaxation processes discussed above.

Next, we have analyzed the θ_E dependence of amplitude A and phase C in YIG (111) shown in Fig. 10 using the same macroscopic model as implemented in YIG (100). To obtain the fourth-rank tensor $\boldsymbol{g}'$ and $\boldsymbol{a}'$ in YIG (111), we can just do rotation operations of the YIG (100) (shown in Appendix E) because only the bulk effect is considered in both samples. The relation between $\boldsymbol{g}$ and $\boldsymbol{g}'$ is as follows:

$$
\begin{aligned}
&g'_{XXXX} = g'_{YYYY} = g'_1 = \frac{1}{2}g_1 + \frac{1}{2}g_2 + g_3 \\
&g'_{XXXZ} = -g'_{XYYZ} = -g'_{YXYZ} = -g'_{YYXZ} = g'_{XXZX} = -g'_{XYZY} = -g'_{YXZY} = -g'_{YYZX} = g'_2 = \frac{\sqrt{2}}{6}g_1 - \frac{\sqrt{2}}{6}g_2 - \frac{\sqrt{2}}{3}g_3 \\
&g'_{XXYY} = g'_{YYXX} = g'_3 = \frac{1}{6}g_1 + \frac{5}{6}g_2 - \frac{1}{3}g_3 \\
&g'_{XXZZ} = g'_{YYZZ} = g'_4 = \frac{1}{3}g_1 + \frac{2}{3}g_2 - \frac{2}{3}g_3 \\
&g'_{XYXY} = g'_{YXXY} = g'_{XYYX} = g'_{YXYX} = g'_5 = \frac{1}{6}g_1 - \frac{1}{6}g_2 + \frac{2}{3}g_3.
\end{aligned}
\tag{18}
$$

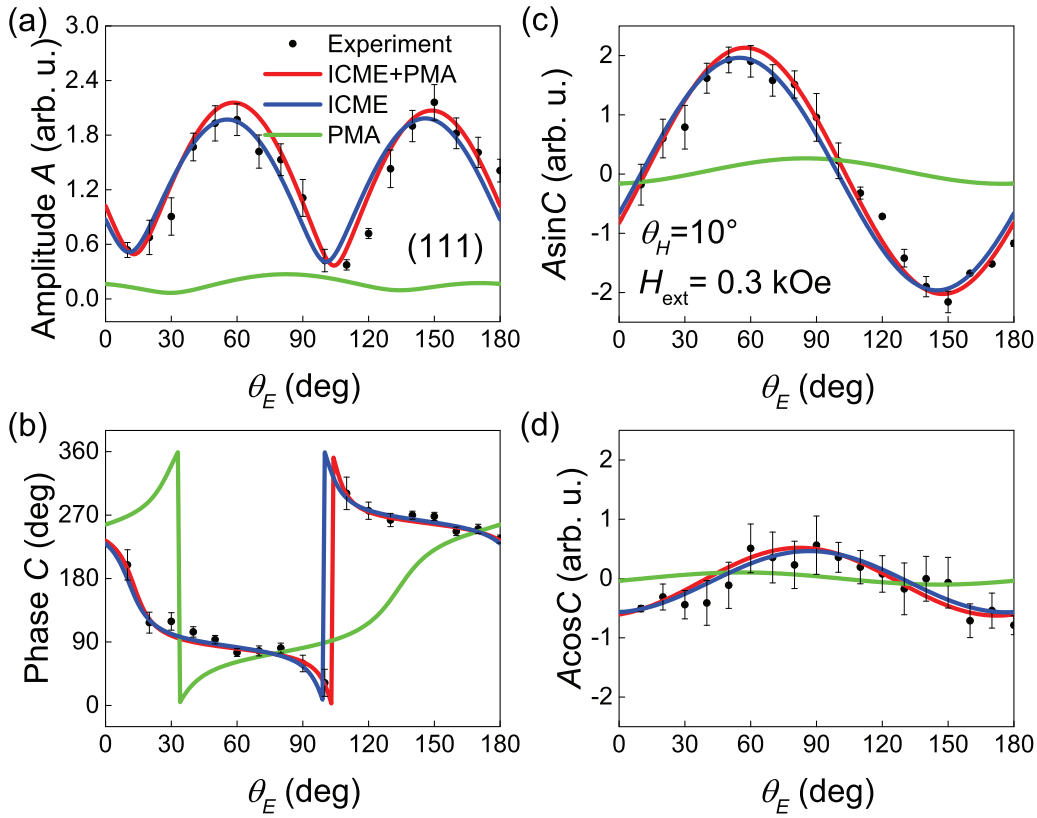

FIG. 10. Polarization direction θ_E dependence of (a) amplitude A, (b) phase C, (c) $A\sin C$, and (d) $A\cos C$ of the $\boldsymbol{M}$ precession in YIG (111). The red lines are fitting curves considering a combination of ICME and PMA; the blue lines and green lines represent the separate contributions of ICME and PMA, respectively.

Thus, $\boldsymbol{H}_{\mathrm{ICME}}$ in YIG (111) can be written as ($\boldsymbol{H}_{\mathrm{PMA}}$ can be obtained by replacing $\boldsymbol{g'}$ with $\boldsymbol{a'}$)

$$(\boldsymbol{H}_{\mathrm{ICME}})_X = \frac{\chi H_{\mathrm{ext}}\mathcal{E}_0^2}{8\pi}\left(\frac{g_1'+g_3'}{2}\cos\theta_1 + \frac{g_1'-g_3'}{2}\cos\theta_1\cos 2\theta_2 + hg_2'\cos 2\theta_2 + g_5'\sin\theta_1\sin 2\theta_2\right), \tag{19a}$$

$$(\boldsymbol{H}_{\mathrm{ICME}})_Y = \frac{\chi H_{\mathrm{ext}}\mathcal{E}_0^2}{8\pi}\left(\frac{g_1'+g_3'}{2}\sin\theta_1 - \frac{g_1'-g_3'}{2}\sin\theta_1\cos 2\theta_2 - hg_2'\sin 2\theta_2 + g_5'\cos\theta_1\sin 2\theta_2\right), \tag{19b}$$

$$(\boldsymbol{H}_{\mathrm{ICME}})_Z = \frac{\chi H_{\mathrm{ext}}\mathcal{E}_0^2}{8\pi}(g_2'\cos\theta_1\cos 2\theta_2 - g_2'\sin\theta_1\sin 2\theta_2 + hg_4'). \tag{19c}$$

We end up with the analytical expression of Eq. (13) in YIG (111) as follows:

$$A\sin C = K(\boldsymbol{u}_1)_Z = K\frac{\chi^2 H_{\mathrm{ext}}\mathcal{E}_0^2}{8\pi}\left[\tau\gamma H_0\left(\frac{g_1'-g_3'}{2}\sin 2\theta_1\cos 2\theta_2 + hg_2'\sin(\theta_1+2\theta_2) - g_5'\cos 2\theta_1\sin 2\theta_2\right)\right.$$
$$\left. + \left(-\frac{h(a_1'-a_3')}{2}\cos 2\theta_1\cos 2\theta_2 - ha_5'\sin 2\theta_1\sin 2\theta_2 - a_2'\cos(\theta_1+2\theta_2) - h\left(\frac{a_1'+a_3'}{2}+a_4'\right)\right)\right], \tag{20a}$$

$$A\cos C = K(\boldsymbol{u}_2)_Z = K\frac{\chi^2 H_{\mathrm{ext}}\mathcal{E}_0^2}{8\pi}\left[\tau\gamma H_0\left(h\frac{g_1'-g_3'}{2}\cos 2\theta_1\cos 2\theta_2 - g_2'\cos(\theta_1+2\theta_2) + hg_5'\sin 2\theta_1\sin 2\theta_2\right)\right.$$
$$\left. + h\left(\frac{g_1'+g_3'}{2}-g_4'\right)\right) + \left(-\frac{a_1'-a_3'}{2}\sin 2\theta_1\cos 2\theta_2 - ha_2'\sin(\theta_1+2\theta_2) + a_5'\cos 2\theta_1\sin 2\theta_2\right)\right]. \tag{20b}$$

We used Eq. (20) and the fitting values of $\boldsymbol{g}$ and $\boldsymbol{a}$ in YIG (100) to fit the θ_E-dependent A and C in YIG (111). The fitting results are reasonably good, as can be seen in Fig. 10.

Based on the above results, we come to the conclusion that the underlying mechanism to stimulate the $\boldsymbol{M}$ precession in YIG (111) is a combination of ICME and PMA, but the ICME is dominant, very similar to YIG (100). However, there exists some difference. The phase C induced by the ICME in YIG (111) changes gradually from 90° to −90° when θ_E is in the range of 90°–120° as shown in Fig. 10(b), whereas it shows

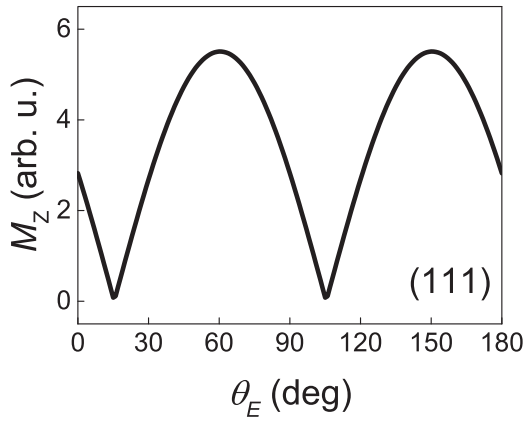

FIG. 11. Calculated z component of $\boldsymbol{M}(t=\tau)$ versus θ_E in YIG (111).

an abrupt change in YIG (100). This is due to the difference of the z component of $\boldsymbol{H}_{\mathrm{ICME}}$. This component in YIG (100) is extremely small, thus having very limited influence on the phase, but it is much larger in YIG (111), as can be seen from the comparison of Eq. (15c) and Eq. (19c). When the in-plane $\boldsymbol{H}_{\mathrm{ICME}}$ and $\boldsymbol{M}$ are nearly parallel for θ_E between 90° and 120°, the M_z component induced by the in-plane $\boldsymbol{H}_{\mathrm{ICME}}$ is small, as shown in Fig. 11. Consequently, the influence of $(\boldsymbol{H}_{\mathrm{ICME}})_z$ on the $\boldsymbol{M}$ precession becomes significant, thus resulting in the large deviation of phase from ±90°. In this case, ICME contributes to both $A\sin C$ and $A\cos C$.

V. CONCLUSIONS

In conclusion, we have demonstrated that in undoped YIG films excited by 400-nm ultrafast laser, only linearly polarized pulses can trigger the coherent $\boldsymbol{M}$ precession. The precession phase and amplitude show strong dependence on the polarization direction. The underlying mechanism is a combination of two distinct nonthermal photomagnetic effects: the impulsive ICME and the displacive PMA. However, the ICME plays the dominant role in the $\boldsymbol{M}$-precession excitation. We can use the same fourth-rank susceptibility tensors to describe the $\boldsymbol{H}_{\mathrm{ICME}}$ and $\boldsymbol{H}_{\mathrm{PMA}}$ in the YIG (100) and YIG (111), indicating that the bulk effect overwhelms the surface effect in the 30-nm-thick YIG films.

ACKNOWLEDGMENTS

This work was supported by the National Key Research and Development Program of China (Grant No. 2016YFA0300703), National Key Basic Research Program of China (Grant No. 2015CB921403), and National Natural Science Foundation of China (Grants No. 11774064 and No. 11727808).

APPENDIX A: THE KITTEL FORMULA IN YIG (100) AND (111)

The in-plane magnetocrystalline anisotropy energies for YIG (100) and YIG (111) are expressed as follows:

$$F_{K(100)} = \frac{K_1}{4}\sin^2 2\theta, \tag{A1a}$$

$$F_{K(111)} = \frac{K_1}{4} + \frac{K_2}{108}(1-\cos 6\theta), \tag{A1b}$$

where θ represents the azimuthal angle of the magnetization $\boldsymbol{M}$, and K_1 and K_2 are magnetic anisotropy constants. It is plausible to neglect the K_2 term in YIG (111) because it is very small. In the case of in-plane external magnetic field $\boldsymbol{H}_{\mathrm{ext}}$, we obtain the precession frequency f for YIG (100) and (111) as follows:

$$f_{(100)} = \gamma\sqrt{\left[H_{\mathrm{ext}}\cos(\xi-\theta)+\left(\frac{2K_1}{\mu_0 M_{\mathrm{s}}}\cos 4\theta\right)\right]\left[H_{\mathrm{ext}}\cos(\xi-\theta)+\left(4\pi M_{\mathrm{s}}+\frac{K_1}{\mu_0 M_{\mathrm{s}}}\left(2-\sin^2 2\theta\right)\right)\right]}\Big/2\pi \tag{A2a}$$

$$f_{(111)} = \gamma\sqrt{[H_{\mathrm{ext}}\cos(\xi-\theta)][H_{\mathrm{ext}}\cos(\xi-\theta)+4\pi M_{\mathrm{s}}]}/2\pi, \tag{A2b}$$

where ξ represents the angle of the external field $\boldsymbol{H}_{\mathrm{ext}}$ with respect to the easy axis, and M_{s} denotes the saturation magnetization.

APPENDIX B: FOURTH-RANK POLAR TENSOR FOR YIG (100)

For crystals with $m3m$ group point, the symmetry operations are as follows:

$\boldsymbol{S}_1$: xy mirror	$\boldsymbol{S}_2$: xz mirror	$\boldsymbol{S}_3$: yz mirror	$\boldsymbol{S}_4$: $C4$ symmetric axis
$\begin{pmatrix}1&0&0\\0&1&0\\0&0&-1\end{pmatrix}$	$\begin{pmatrix}1&0&0\\0&-1&0\\0&0&1\end{pmatrix}$	$\begin{pmatrix}-1&0&0\\0&1&0\\0&0&1\end{pmatrix}$	$\begin{pmatrix}\cos\theta_{\mathrm{R}}&-\sin\theta_{\mathrm{R}}&0\\\sin\theta_{\mathrm{R}}&\cos\theta_{\mathrm{R}}&0\\0&0&1\end{pmatrix}$

where θ_{R} is $360^\circ/\mathrm{n}$ for the C_{n} symmetric axis.

The elements of fourth-rank polar tensor $\boldsymbol{g}$ stay unchanged for the symmetry operation $\boldsymbol{S}$,

$$g_{i'j'k'l'} = \sum S_{i'i} S_{j'j} S_{k'k} S_{l'l} g_{ijkl}. \tag{B1}$$

Applying the operations of $\boldsymbol{S_1}$–$\boldsymbol{S_4}$, we found only three nonzero independent components,

$$\begin{aligned} &g_{xxxx} = g_{yyyy} = g_1 \\ &g_{xxyy} = g_{yyxx} = g_{xxzz} = g_{yyzz} = g_2 \\ &g_{xyxy} = g_{yxxy} = g_{xyyx} = g_{yxyx} = g_3. \end{aligned} \tag{B2}$$

APPENDIX C: CONVERSION BETWEEN $\{x, y, z\}$ AND $\{X, Y, Z\}$ IN YIG (100)

For YIG (100), X-, Y-, and Z-axes represents $[01\bar{1}]$, [011], and [100], respectively. x-, y-, and z-axes represent [010], [001], and [100], respectively. According to the crystal symmetry, g_{ijkl} under $\{X, Y, Z\}$ can be written as

$$\begin{aligned} &g_{XXXX} = g_{YYYY} = g_{1'} \\ &g_{XXYY} = g_{YYXX} = g_{2'} \\ &g_{XXZZ} = g_{YYZZ} = g_{3'} \\ &g_{XYXY} = g_{YXXY} = g_{XYYX} = g_{YXYX} = g_{4'}. \end{aligned} \tag{C1}$$

The absolute value of a physical quantity should maintain unchanged after the transformation of the coordinate system. The transformation matrix for rotation by a counterclockwise angle θ_R is

$$\boldsymbol{R}_\theta = \begin{pmatrix} \cos\theta_R & \sin\theta_R & 0 \\ -\sin\theta_R & \cos\theta_R & 0 \\ 0 & 0 & 1 \end{pmatrix}. \tag{C2}$$

By applying the angle $\theta_R = \beta = 45^\circ$ into the rotation operation between $\{X, Y, Z\}$ and $\{x, y, z\}$, we obtain the relationship of the g_{ijkl} in two different coordinate systems as follows:

$$\begin{aligned} &g_{xxxx} = g_{yyyy} = g_1 = \tfrac{1}{2}g_{1'} + \tfrac{1}{2}g_{2'} + g_{4'} \\ &g_{xxyy} = g_{yyxx} = g_2 = \tfrac{1}{2}g_{1'} + \tfrac{1}{2}g_{2'} - g_{4'} \\ &g_{xxzz} = g_{yyzz} = g_2 = g_{3'} \\ &g_{xyxy} = g_{yxxy} = g_{xyyx} = g_{yxyx} = g_3 = \tfrac{1}{2}g_{1'} - \tfrac{1}{2}g_{2'}. \end{aligned} \tag{C3}$$

Then we obtain the expanded expression for Eq. (13) in $\{X, Y, Z\}$:

$$\begin{aligned} A\sin C = K(\boldsymbol{u}_1)_Z = K\frac{\chi^2 H_{\text{ext}}\mathcal{E}_0^2}{8\pi}\Bigg[&\left(\tau\gamma H_{\text{ext}}\frac{g_{1'}-g_{2'}}{2}\sin 2\theta_{1'}\cos 2\theta_{2'} - \tau\gamma H_{\text{ext}} g_{4'}\cos 2\theta_{1'}\sin 2\theta_{2'}\right) \\ &+ \left(-\frac{h(a_{1'}-a_{2'})}{2}\sin 2\theta_{1'}\cos 2\theta_{2'} - h a_{4'}\sin 2\theta_{1'}\sin 2\theta_{2'} - h\left(\frac{a_{1'}+a_{2'}}{2}+a_{3'}\right)\right)\Bigg], \end{aligned} \tag{C4}$$

$$\begin{aligned} A\cos C = K(\boldsymbol{u}_2)_Z = K\frac{\chi^2 H_{\text{ext}}\mathcal{E}_0^2}{8\pi}\Bigg[&\left(h\tau\gamma H_{\text{ext}}\frac{g_{1'}-g_{2'}}{2}\sin 2\theta_{1'}\cos 2\theta_{2'} + h\tau\gamma H_{\text{ext}} g_{4'}\sin 2\theta_{1'}\sin 2\theta_{2'}\right. \\ &\left. + h\tau\gamma H_{\text{ext}}\left(\frac{g_{1'}+g_{2'}}{2}-g_{3'}\right)\right) + \left(-\frac{a_{1'}-a_{2'}}{2}\sin 2\theta_{1'}\cos 2\theta_{2'} + a_{4'}\cos 2\theta_{1'}\sin 2\theta_{2'}\right)\Bigg] \end{aligned} \tag{C5}$$

By considering $\theta_{1'} = \theta_1 - \beta$, $\theta_{2'} = \theta_2 - \beta$ and $z \parallel Z$, the expressions of perpendicular components of $\boldsymbol{u}$ in $\{x, y, z\}$ and $\{X, Y, Z\}$ coordinate systems are identical.

APPENDIX D: g AND a PARAMETERS

The fitting parameters of $\boldsymbol{g}$ and $\boldsymbol{a}$ for YIG (100) and YIG (111) are as follows:

g_1	g_2	g_3	a_1	a_2	a_3
107145	59525	14880	0.8	0.5	−0.2

The parameters of $\boldsymbol{g'}$ and $\boldsymbol{a'}$ for YIG (111) calculated from $\boldsymbol{g}$ and $\boldsymbol{a}$ are as follows:

g'_1	g'_2	g'_3	g'_4	g'_5
98215	−4209.6	62501.7	65478.3	17856.7
a'_1	a'_2	a'_3	a'_4	a'_5
0.45	−0.16	0.62	−0.73	−0.08

APPENDIX E: ROTATION OPERATIONS BETWEEN YIG (100) AND YIG (111)

We obtain $g'_{i'j'k'l'}$ in $\{X, Y, Z\}$ of YIG (111) from g_{ijkl} in $\{x, y, z\}$ of YIG (100) using $g'_{i'j'k'l'} = \sum R_{i'i} R_{j'j} R_{k'k} R_{l'l} g_{ijkl}$ with $\boldsymbol{R} = \boldsymbol{R}_z \boldsymbol{R}_y \boldsymbol{R}_x$. Here, $\boldsymbol{R}_z$ rotates $\{x, y, z\}$ to $\{x_1, y_1, z_1\}$ around the z axis by the angle θ_{R3}. $\boldsymbol{R}_y$ rotates $\{x_1, y_1, z_1\}$ to $\{x_2, y_2, z_2\}$ around the y_1 axis by the angle θ_{R2}. $\boldsymbol{R}_z$ rotates $\{x_2, y_2, z_2\}$ to $\{X, Y, Z\}$ around the x_2 axis by the angle θ_{R1}.

$\boldsymbol{R}_z$	$\boldsymbol{R}_y$	$\boldsymbol{R}_x$
$\begin{pmatrix} \cos\theta_{R3} & \sin\theta_{R3} & 0 \\ -\sin\theta_{R3} & \cos\theta_{R3} & 0 \\ 0 & 0 & 1 \end{pmatrix}$	$\begin{pmatrix} \cos\theta_{R2} & 0 & -\sin\theta_{R2} \\ 0 & 1 & 0 \\ \sin\theta_{R2} & 0 & \cos\theta_{R2} \end{pmatrix}$	$\begin{pmatrix} 1 & 0 & 0 \\ 0 & \cos\theta_{R1} & \sin\theta_{R1} \\ 0 & -\sin\theta_{R1} & \cos\theta_{R1} \end{pmatrix}$

Converting from $\{x, y, z\}$ in YIG (100) to $\{X, Y, Z\}$ in YIG (111), we have $\theta_{R3} = 45^\circ$, $\theta_{R2} = \cos^{-1}\frac{\sqrt{3}}{3}$, and $\theta_{R1} = 0^\circ$. Hence, the total rotation operation can be written as

$$R = \begin{pmatrix} \cos\theta_{R2}\cos\theta_{R3} & \cos\theta_{R2}\sin\theta_{R3} & -\sin\theta_{R2} \\ \sin\theta_{R1}\sin\theta_{R2}\cos\theta_{R3} - \cos\theta_{R1}\sin\theta_{R3} & \sin\theta_{R1}\sin\theta_{R2}\sin\theta_{R3} + \cos\theta_{R1}\cos\theta_{R3} & \sin\theta_{R1}\cos\theta_{R2} \\ \cos\theta_{R1}\sin\theta_{R2}\cos\theta_{R3} + \sin\theta_{R1}\sin\theta_{R3} & \cos\theta_{R1}\sin\theta_{R2}\sin\theta_{R3} - \sin\theta_{R1}\cos\theta_{R3} & \cos\theta_{R1}\cos\theta_{R2} \end{pmatrix}$$
$$= \begin{pmatrix} \frac{\sqrt{6}}{6} & -\frac{\sqrt{2}}{2} & \frac{\sqrt{3}}{3} \\ \frac{\sqrt{6}}{6} & \frac{\sqrt{2}}{2} & \frac{\sqrt{3}}{3} \\ -\frac{\sqrt{6}}{3} & 0 & \frac{\sqrt{3}}{3} \end{pmatrix}. \tag{E1}$$

[1] Y. Kato, R. C. Myers, A. C. Gossard, and D. D. Awschalom, Nature (London) **427**, 50 (2004).
[2] H. Ohno, D. Chiba, F. Matsukura, T. Omiya, E. Abe, T. Dietl, Y. Ohno, and K. Ohtani, Nature (London) **408**, 944 (2000).
[3] T. Lottermoser, T. Lonkai, U. Amann, D. Hohlwein, J. Ihringer, and M. Fiebig, Nature (London) **430**, 541 (2004).
[4] A. Asamitsu, Y. Tomioka, H. Kuwahara, and Y. Tokura, Nature (London) **388**, 50 (1997).
[5] A. V. Kimel, A. Kirilyuk, P. A. Usachev, R. V. Pisarev, A. M. Balbashov, and Th. Rasing, Nature (London) **435**, 655 (2005).
[6] Y. Hashimoto, S. Kobayashi, and H. Munekata, Phys. Rev. Lett. **100**, 067202 (2008).
[7] A. Kirilyuk, A. V. Kimel, and Th. Rasing, Rev. Mod. Phys. **82**, 2731 (2010).
[8] E. Beaurepaire, J. C. Merle, A. Daunois, and J. Y. Bigot, Phys. Rev. Lett. **76**, 4250 (1996).
[9] G. P. Zhang and W. Hübner, Phys. Rev. Lett. **85**, 3025 (2000).
[10] J. Hohlfeld, E. Matthias, R. Knorren, and K. H. Bennemann, Phys. Rev. Lett. **78**, 4861 (1997).
[11] G. Ju, A. V. Nurmikko, R. F. C. Farrow, R. F. Marks, M. J. Carey, and B. A. Gurney, Phys. Rev. B **58**, R11857 (1998).
[12] A. V. Kimel, A. Kirilyuk, A. Tsvetkov, R. V. Pisarev, and Th. Rasing, Nature (London) **429**, 850 (2004).
[13] G. Ju, J. Hohlfeld, B. Bergman, R. J. M. v. d. Veerdonk, O. N. Mryasov, J.-Y. Kim, X. Wu, D. Weller, and B. Koopmans, Phys. Rev. Lett. **93**, 197403 (2004).
[14] M. B. Agranat, S. I. Ashitkov, A. B. Granovskii, and G. I. Rukman, Zh. Eksp. Teor. Fiz. **86**, 1376 (1984) [Sov. Phys. JETP **59**, 804 (1984)].
[15] M. B. Agranat, S. I. Anhitkov, A. V. Kirillin, V. E. Fortov, S. I. Anislmov, A. B. Granovskiį, and P. S. Kondratenko, JETP Lett. **67**, 953 (1998).
[16] N. Del Fatti, C. Voisin, M. Achermann, S. Tzortzakis, D. Christofilos, and F. Vallée, Phys. Rev. B **61**, 16956 (2000).
[17] J. Hohlfeld, T. Gerrits, M. Bilderbeek, Th. Rasing, H. Awano, and N. Ohta, Phys. Rev. B **65**, 012413 (2001).
[18] A. V. Kimel, A. Kirilyuk, F. Hansteen, R. V. Pisarev, and Th. Rasing, J. Phys.: Condens. Matter **19**, 043201 (2007).
[19] A. F. Kabychenkov, Zh. Eksp. Teor. Fiz. **100**, 1219 (1991) [Sov. Phys. JETP **73**, 672 (1991)].
[20] V. F. Kovalenko and É. L. Nagaev, Sov. Phys. Usp. **29**, 297 (1986).
[21] R. W. Teale, D. W. Temple, U. Enz, and R. F. Pearson, J. Appl. Phys. **40**, 1435 (1969).
[22] R. Metselaar, M. A. H. Huyberts, and H. Logmans, J. Appl. Phys. **46**, 3171 (1975).
[23] F. Hansteen, A. Kimel, A. Kirilyuk, and Th. Rasing, Phys. Rev. Lett. **95**, 047402 (2005).
[24] P. S. Pershan, J. P. V. D. Ziel, and L. D. Malmstrom, Phys. Rev. **143**, 574 (1966).
[25] V. N. Gridnev, Phys. Rev. B **77**, 094426 (2008).
[26] A. M. Kalashnikova, A. V. Kimel, R. V. Pisarev, V. N. Gridnev, P. A. Usachev, A. Kirilyuk, and Th. Rasing, Phys. Rev. B **78**, 104301 (2008).
[27] A. M. Kalashnikova, A. V. Kimel, R. V. Pisarev, V. N. Gridnev, A. Kirilyuk, and Th. Rasing, Phys. Rev. Lett. **99**, 167205 (2007).
[28] R. Iida, T. Satoh, T. Shimura, K. Kuroda, B. A. Ivanov, Y. Tokunaga, and Y. Tokura, Phys. Rev. B **84**, 064402 (2011).
[29] A. V. Kimel, C. D. Stanciu, P. A. Usachev, R. V. Pisarev, V. N. Gridnev, A. Kirilyuk, and Th. Rasing, Phys. Rev. B **74**, 060403 (2006).
[30] C. A. Perroni and A. Liebsch, Phys. Rev. B **74**, 134430 (2006).
[31] F. Hansteen, A. Kimel, A. Kirilyuk, and Th. Rasing, Phys. Rev. B **73**, 014421 (2006).

[32] T. Satoh, N. P. Duong, and M. Fiebig, Phys. Rev. B **74**, 012404 (2006).
[33] M. Fiebig, N. Phuc Duong, T. Satoh, B. B. Van Aken, K. Miyano, Y. Tomioka, and Y. Tokura, J. Phys. D: Appl Phys. **41**, 164005 (2008).
[34] D. M. Wang, Y. H. Ren, X. Liu, J. K. Furdyna, M. Grimsditch, and R. Merlin, Phys. Rev. B **75**, 233308 (2007).
[35] M. van Kampen, C. Jozsa, J. T. Kohlhepp, P. LeClair, L. Lagae, W. J. M. de Jonge, and B. Koopmans, Phys. Rev. Lett. **88**, 227201 (2002).
[36] J. Wang, I. Cotoros, D. S. Chemla, X. Liu, J. K. Furdyna, J. Chovan, and I. E. Perakis, Appl. Phys. Lett. **94**, 021101 (2009).
[37] G. Winkler, *Magnetic Garnets* (Vieweg, Braunschweig, 1981).
[38] P. Hansen and A. Paoletti, *Physics of Magnetic Garnets* (North-Holland, Amsterdam, 1978).
[39] I. Yoshimine, T. Satoh, R. Iida, A. Stupakiewicz, A. Maziewski, and T. Shimura, J. Appl. Phys. **116**, 043907 (2014).
[40] T. Satoh, Y. Terui, R. Moriya, B. A. Ivanov, K. Ando, E. Saitoh, T. Shimura, and K. Kuroda, Nat. Photonics **6**, 662 (2012).
[41] Y. Hashimoto, S. Daimon, R. Iguchi, Y. Oikawa, K. Shen, K. Sato, D. Bossini, Y. Tabuchi, T. Satoh, B. Hillebrands, G. E.W. Bauer, T. H. Johansen, A. Kirilyuk, T. Rasing, and E. Saitoh, Nat. Commun. **8**, 15859 (2017).
[42] V. G. Veselago, R. A. Doroshenko, and S. G. Rudov, Zh. Eksp. Teor. Fiz. **105**, 638 (1994) [JETP **78**, 341 (1994)].
[43] G. F. Dionne and G. A. Allen, J. Appl. Phys. **73**, 6127 (1993).
[44] A. Stupakiewicz, A. Maziewski, I. Davidenko, and V. Zablotskii, Phys. Rev. B **64**, 064405 (2001).
[45] M. Deb, M. Vomir, J. L. Rehspringer, and J. Y. Bigot, Appl. Phys. Lett. **107**, 252404 (2015).
[46] F. Atoneche, A. M. Kalashnikova, A. V. Kimel, A. Stupakiewicz, A. Maziewski, A. Kirilyuk, and Th. Rasing, Phys. Rev. B **81**, 214440 (2010).
[47] R. Alben, E. M. Gyorgy, J. F. Dillon, and J. P. Remeika, Phys. Rev. B **5**, 2560 (1972).
[48] V. E. Zakharov and E. A. Kuznetsov, Usp. Fiz. Nauk **167**, 1137 (1997).
[49] Y.-X. Yan, E. B. Gamble Jr., and K. A. Nelson, J. Chem. Phys. **83**, 5391 (1985).
[50] L. P. Pitaevskii, Sov. Phys. JETP **12**, 1008 (1961).
[51] Y. R. Shen and N. Bloembergen, Phys. Rev. **143**, 372 (1966).
[52] S. G. Rudov, V. V. Verchenko, K. Veselago, A. Maziewski, M. Tekielak, S. N. Lyakhimets, and J. M. Desvignes, IEEE Trans. Magn. **30**, 791 (1994).
[53] V. V. Eremenko, S. L. Gnatchenko, I. S. Kachur, V. G. Piryatinskaya, A. M. Ratner, and V. V. Shapiro, Phys. Rev. B **61**, 10670 (2000).
[54] B. A. Zon, V. Ya. Kupershmidt, G. V. Pakhomov, and T. T. Urazbaev, Pis'ma Zh. Eksp. Teor. Fiz. **45**, 219 (1987) [JETP Lett. **45**, 272 (1987)].
[55] T. E. Stevens, J. Kuhl, and R. Merlin, Phys. Rev. B **65**, 144304 (2002).
[56] M. G. Cottam and D. J. Lockwood, *Light Scattering in Magnetic Solids* (Wiley, New York, 1986).
[57] P. S. Pershan, Phys. Rev. **130**, 919 (1963).
[58] A. B. Chizhik, I. I. Davidenko, A. Maziewski, and A. Stupakiewicz, Phys. Rev. B **57**, 14366 (1998).
[59] D. P. Landau, K. Binder, C. Rovelli, and F. Vidotto, *About Physics* (Cambridge University Press, Cambridge, 1988).
[60] B. Hillebrands and K. Ounadjela, *Spin Dynamics in Confined Magnetic Structures II* (Springer, Berlin, 2003).
[61] T. P. Ma, S. F. Zhang, Y. Yang, Z. H. Chen, H. B. Zhao, and Y. Z. Wu, J. Appl. Phys. **117**, 013903 (2015).
[62] J. F. B. Hawkes and R. W. Teale, J. Phys. C: Solid State Phys. **5**, 481 (1972).